Ocean Engineering 249 (2022) 110935

Contents lists available at ScienceDirect

Ocean Engineering

journal homepage: www.elsevier.com/locate/oceaneng

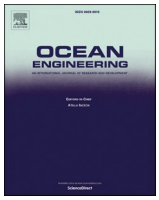

Large-scale shear test of brash ice

Aniket Patil [a,b,*], Vasiola Zhaka [b], Bjørnar Sand [a], Jan Laue [b], Andrzej Cwirzen [b]

[a] SINTEF Narvik, Norway
[b] Luleå University of Technology, Luleå, Sweden

ARTICLE INFO

Keywords:
Large-scale shear
Brash ice
Volumetric strain
Continuous Surface Cap Model (CSCM)

ABSTRACT

A large-scale shear apparatus has been originally developed and built to test the mechanical properties of coarse-grained material. It was used to evaluate the shear behaviour of brash ice. The brash ice blocks were collected at Luleå harbour in two separate measuring campaigns in March 2020 and March 2021. The shear cylinder was loaded with brash ice in Luleå port in two different locations for the two test campaigns, and the displacement-controlled shear tests were conducted. A vertical actuator was used to set a constant normal load and then a horizontal actuator was used to move the shear swing. In this setup, time, forces, and displacements were recorded at the forward and return stroke of the horizontal actuator. In total 6 shear cycles on two brash ice samples with axial stress of 4.8 kPa, 2 kPa and 1 kPa were performed. The test data was analysed to determine the relationship between shear stress and shear strain. The macro-porosity and confining axial force were found to be the most influential factors in determining the strength and deformation of the brash ice. Furthermore, an attempt has been made to estimate a few parameters of a material model known as the Continuous Surface Cap Model.

1. Introduction

The ice channels in ice-covered waters are made and maintained by icebreaking operations. These channels are filled with ice floes and broken ice blocks often called brash ice. To ensure safe navigation in brash ice channels, vessels must be constructed to overcome the ice resistance, and they must comply with the ice class rules. The Finnish-Swedish ice class rules (FSICR) define the requirement of a vessel for a certain ice class based on brash ice channel thickness and width. The ice-class rules define ice conditions and the minimum engine power requirements which ensures that the vessel can withstand and overcome the ice resistance. The brash ice accumulation causes increased vessel resistance and impedes access to ports and harbours. As defined by Mellor (1980) and Greisman (1981), brash ice is a granular material and generally, no significant cohesion is found between the ice blocks. The ice blocks are mainly less than 2 m. With repeated vessel passage the ice blocks are milled and become rounder. The reported macro-porosity for brash ice is usually above 20%, see Bonath et al. (2019) and Matala (2021). After every vessels passage, some ice blocks are pushed sideways and may form ridge-like structures. The negative air temperatures and the presence of water-filled pores complicate further the nature of brash ice. The consequences of which are initially the formation of freeze bonds and subsequently the brash ice consolidation. The brash ice accumulations make the winter navigation in Gulf of Bothnia and the Gulf of Finland challenging and unsafe. Hence, understanding the properties and failure mechanics of brash ice is crucial to essential maritime activities.

In the past majority of research related to the brash ice was focused on: macro-porosity, cohesion, angle of internal friction, compressive strength, and ice block's size and distribution. The aim has been to define and to understand brash ice formation and its failure mechanics, see Tuovinen (1979), Sandkvist (1981). The ice channel resistance developed on hulls of passing vessels can be broken down into three major components: [1] energy needed to move the ice blocks [2] compaction of loose ice mass [3] friction between vessels and ice [4] speed dependency component, see Kitazawa and Ettema (1985), Ettema et al. (1985), Ettema et al. (1986), Ettema et al. (1998), Hu and Zhou (2015) and Matala and Skogström (2017). Full-scale measurements performed on brash ice channels have been reported by Riska et al. (2019), Bonath et al. (2019), and Zhaka et al. (2020). Due to the similarity between ice rubble and brash ice, the brash ice testing is often interchangeable with ice rubble testing. However, the ice blocks in ridge keels have a more angular shape while the size of ice blocks can be larger.

* Corresponding author. SINTEF Narvik, Norway.
E-mail address: aniket.patil@sintef.no (A. Patil).

https://doi.org/10.1016/j.oceaneng.2022.110935
Received 5 July 2021; Received in revised form 18 February 2022; Accepted 21 February 2022
Available online 2 March 2022

The shear box tests are often used to study the shear properties of ice rubble. They enable to study of the relationship between the cohesion and the internal friction angle. However, to represent realistic ice conditions and to interpret the results, tests require a considerable understanding of the failure process. As shown by Polojärvi et al. (2015), the peak loads measured in the shear box experiments are due to force chains that form during shear deformation. These peak load values are limited by the buckling of the force chains. The shear box test data can be fitted to Mohr-Coulomb failure criterion based on peak forces but cannot cover the post-peak behaviour, e.g. compaction. Small scale shear box tests have been performed using scaled-down ice blocks, see Pustogvar et al. (2014). The shear box tests have been used to determine the role of angle of internal friction, cohesion formed due to freeze-bond, and normal pressure on shear properties, Fransson and Sandkvist (1985) and Serré et al. (2011). Whereas, the in-situ tests like the punch through tests showed the influence of cohesion in the first shear failure mode, see Heinonen and Määttänen (2001). The interpretation of those test results can be found elsewhere, see Liferov and Bonnemaire (2005). The triaxial compression tests were performed to investigate the strength and the deformation behaviour of crushed ice by Singh and Jordaan (1996). It was concluded that the strength is depended on macro-porosity, loading rate and confining pressure. However, Gale et al. (1987) showed that peak strength is unaffected by loading rate whereas Spencer et al. (1991) underlined the importance of volumetric strain measurements in their triaxial compression tests. All the above-mentioned triaxial tests were performed on broken or crushed ice sample sizes having diameters 65–75 mm and lengths 75–150 mm. Therefore, appropriate scaling laws should be used to extrapolate the ice strength. Timco et al. (1992) have examined the influence of block sizes, block shapes and condition of rubble (wet or dry) using the bi-axial compression apparatus. In order to study the mechanical properties of model ice rubble, Serré (2011) has carried out oedometer tests, piling tests, and punch tests. Furthermore, Matala (2021) studied porosity, block size and distribution, the angle of repose, compressibility, and angle of internal friction of brash ice by using different measurement devices, including the shear box device and the compressibility measurement device.

The broken ice blocks form an interfacial layer between the parent ice sheet and the structure, due to extensive cracking and fragmentation of the parent ice sheet. This zone of broken ice blocks has high macro-porosity, see Jordaan and Timco (1988). The total force on the structure is mostly controlled by mechanical and physical properties of this broken ice mass, structure stiffness, ice inhomogeneity, and velocity of the interaction. Often the failure process of this high porosity ice layer begins with collapsing of pores and continues with microcracks formation at the grain boundaries. These two failure processes often give two distinctive peaks observed in strength tests, see Jordaan and Singh (1994), Jordaan (2001) and Dempsey et al. (2001). A layer of broken ice can form between a parent ice sheet and a ship's hull when a ship passes through a brash ice channel, which creates similar boundary conditions mentioned above. Therefore, it is necessary to study the volumetric response of broken ice mass under compressive and shear stress state.

The tests listed above are rare and infrequent. Many authors have acknowledged the knowledge gaps in brash ice testing including Sorsimo et al. (2014) and Li et al. (2018). Also, the tests are highly dependent on the apparatus used. The stiffness of the apparatus and resistance of the loading mechanism should be carefully dealt with while post-processing test data. Furthermore as shown by Matala (2021), the model ice can be softer and consist of slush. This may deviate from real brash ice properties. Therefore, the testing of the behaviour of brash ice in large scale shearing apparatus is proposed. A large-scale triaxial shear testing apparatus used in current testing was built and developed at Luleå University of Technology (LTU). The large-scale shear apparatus is an up-scaled direct shear apparatus. The equipment is designed for testing coarse soils and crushed rock materials. One of the advantages of the large-scale shear test is that the measurement of volume changes is more accurate than the direct shear test. Two separate measuring campaigns in March 2020 and March 2021 were conducted to estimate the properties of brash ice using a large-scale shear testing apparatus. The testing procedures were essentially the same for both years except for sampling areas. This paper describes large-scale shear tests conducted on brash ice. The main objectives of these tests were to assess the experimental techniques, and to study the behaviour of brash ice in a large-scale shear test.

2. Test setup and procedure

The large-scale shearing apparatus consists of a vertical actuator attached to the loading frame at the top part. Whereas the horizontal actuator is attached to a shear swing which is suspended with four rods. The rods carry the weight of the sample body when mounted. The steel wire reinforced rubber membrane is attached to the top and bottom mount ring. A simple sketch for the apparatus is given in Fig. 2. The sample body consists of a rubber membrane which is attached at the bottom to the shear swing and the top part is fixed to a rigid frame. The diameter of the membrane cylinder is 1 m and it has an effective height of 1 m. The brash ice blocks were collected at Luleå harbour and then loaded into a shear cylinder. All tests were conducted on the same day to avoid any change in ice properties due to exposure to temperatures above zero. The testing procedure can be divided into four stages. The first stage was the loading of ice blocks into the membrane cylinder. The membrane cylinder was filled with ice blocks collected from the Luleå harbour by crane. The harbour was not navigated the last 9 h before the collection. The ice blocks were broken intensively inside the cylinder to uniformly distribute the ice mass, see Fig. 1 (c). Then shear cylinder was transported back to LTU with an open truck.

In the second stage, the rubber membrane cylinder was filled with ice blocks and mounted in the shear swing. The side heights of the cell were registered. The top of the rubber membrane was carefully adjusted to have a rather flat surface. In the third stage, a vertical load was applied to set the constant level of the vertical force. Although the tests were conducted in a relatively shorter time window, the possibility of the formation of freeze bonds due to sintering cannot be ruled out. The experimental study by Boroojerdi et al. (2020) showed that the sintering-creep mechanism can lead to the development of freeze bond strength. All tests were carried out in dry condition meaning air was the only pore fluid. Lastly, the horizontal actuator was moved to a certain displacement and then returned to its original position with constant speed. The force was registered in the forward and return stroke of the horizontal actuator. The chosen shearing speed was assumed to be slow enough not to generate any pore pressure, enabling the blocks to rearrange during the shearing. The rubber membrane is reinforced with steel wires and has some resistance which needed to be retracted from each test's results.

The horizontal force, vertical forces and associated displacements of actuators were registered. In the measuring campaign of March 2021, a change in circumference was measured by a wire gauge placed around the membrane cylinder. The circumference was measured in the middle of the membrane, see Fig. 3 (c). It is assumed that the change in circumference at the ends is unaffected by the testing. The photographs of the large-scale shear apparatus in action are shown in Fig. 3. Due to logistic constraints, only one brash ice sample was used in each test campaign. The axial stress was calculated by dividing the axial force by the area of the sample. The change in height of the sample was estimated based on the vertical stroke of the piston and circumferential measurements were used to calculate the change in radius of the sample. Both measurements were used to estimate the volume change. Two thermocouples were mounted on the surface and depth of 55 cm. The macro-porosity was calculated using the final volume of the test cylinder and weight before shearing.

Additionally, few ice blocks were collected for further testing. Fig. 4 shows the sampling areas and the brash ice microstructure from the different campaigns. The brash ice accretion in year 2020 was lower

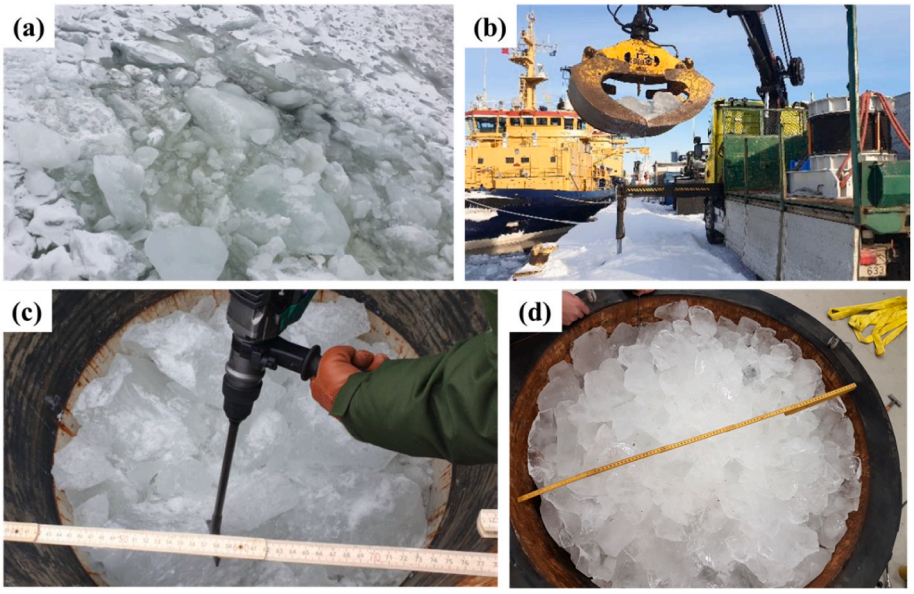

Fig. 1. Photos taken during brash ice sampling show, (a) the sampling area in March 2021 (b) filling of the membrane by using crane (c) crushing of ice blocks while filling (d) the ice-filled membrane.

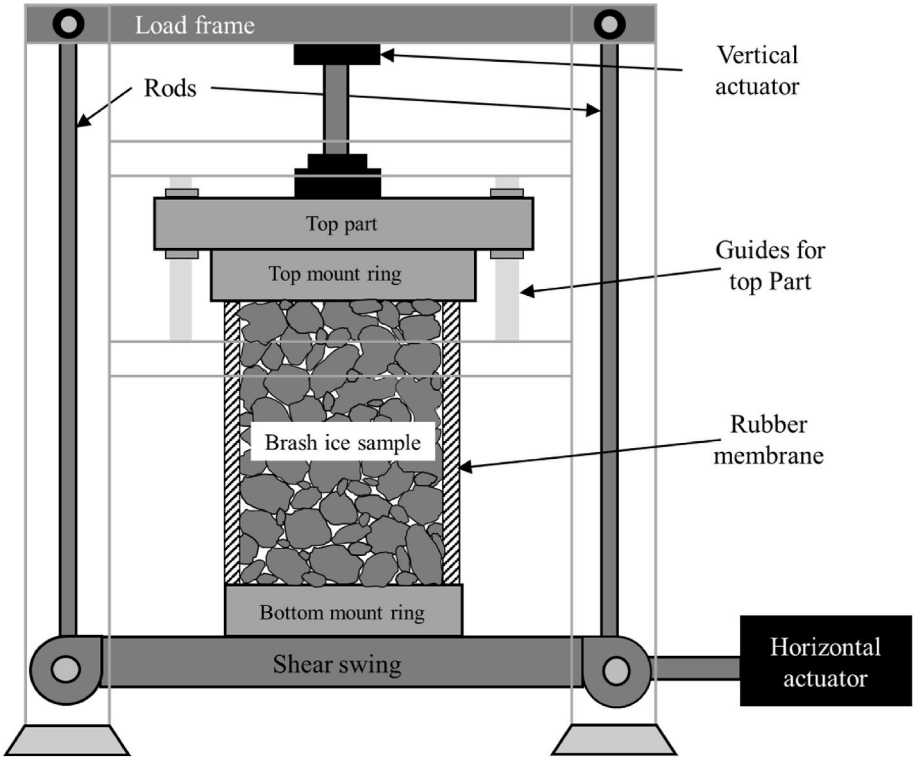

Fig. 2. Sketch of large-scale shear test apparatus (not to the scale).

than in year 2021. The frequently used ports contain smaller blocks with rounder shapes. The microstructure of ice samples was determined by examining thin sections under cross-polarized light, see Fig. 4. There was mainly columnar ice with a c-axis oriented both vertically and horizontally. In addition to snow ice, a mix of columnar and granular ice was observed in smaller fractions. In the year 2020, columnar ice or ice with larger crystals dominates the microstructure as the brash ice still retains the characteristics of the parent ice sheet. While in year 2021, the ice consists of small randomly oriented crystals that represent the breaking and refreezing of ice.

2.1. Post-processing of test data

A MATLAB script was written to import and post-processes the raw test data. As the sampling rate was not high enough, linear interpolation was performed. Before the application of the horizontal force, the vertical force was applied and held constant at the set value. When the brash ice sample was subjected to vertical force, it went through a deformation process which resembles that of a confined uniaxial compression. This information can be exploited further to estimate the secant elastic modulus. The brash ice sample, being a granular material,

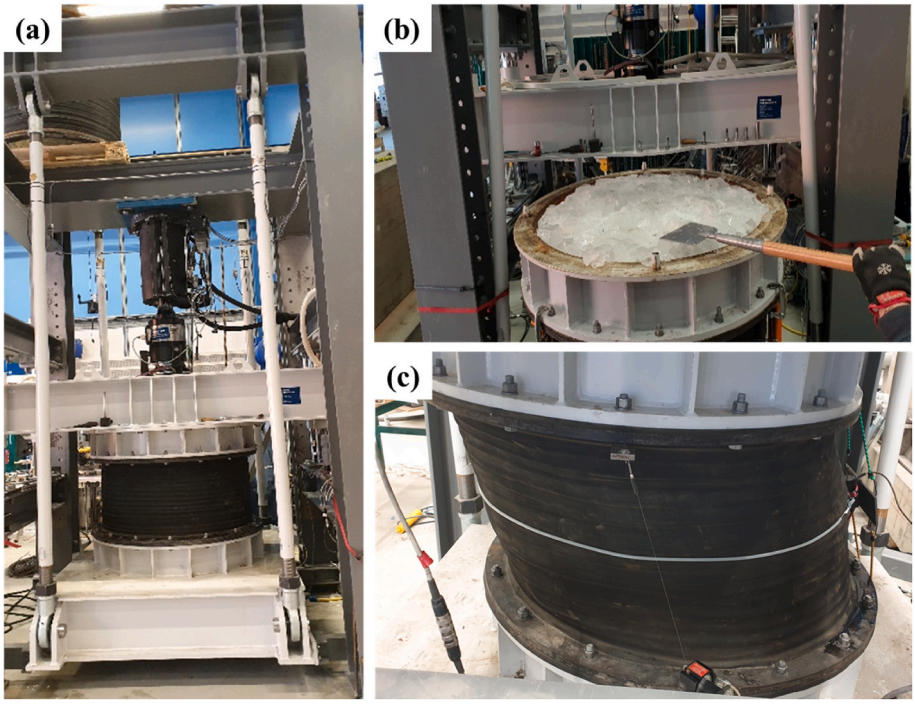

Fig. 3. Photos showing (a) the large-scale shearing apparatus (b) compaction prior to shearing (c) the placement of wire gauges to measure the circumference and length of the rubber membrane at the deformed position.

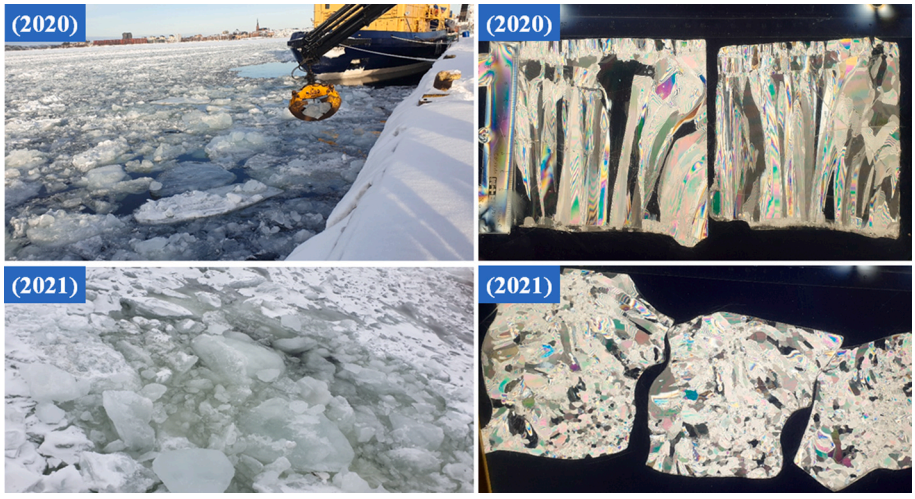

Fig. 4. Photos showing the sampling area [left side] and examples of the microstructure [right side] of ice blocks collected in year 2020 and 2021.

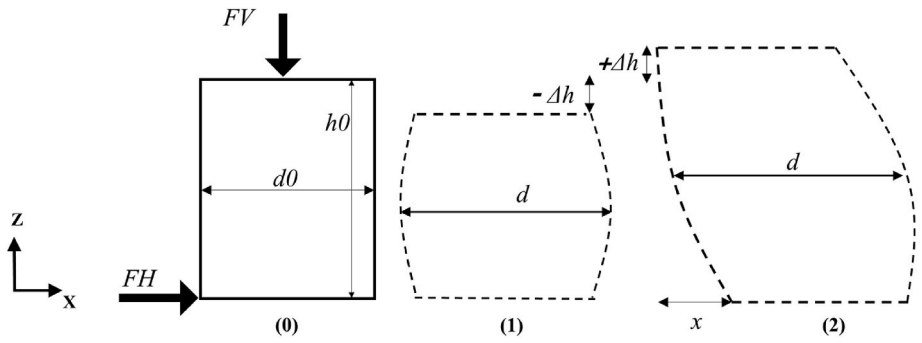

Fig. 5. A Simplified sketch showing three phases of test mechanics, [0] initial, [1] compaction and [3] shearing.

goes through volumetric expansion or dilation as sheared. The cross-sectional area A at any stage during shear can be determined assuming that the sample remains cylindrical. Let Δh_0 be the change in height and ΔV_0 be the volume change. The volume of the sample at any stage is given by $V_0 \pm \Delta V_0$. A simplified sketch showing test mechanics is illustrated in Fig. 5, where F_H and F_V are the horizontal and vertical force components, d and d_0 are the final and initial sample diameter measured at the middle of the membrane and $h0$ and Δh are the initial height and change in height respectively.

The following equation can be used to calculate the shear area A of the brash ice sample

$$A = A_0 \frac{\left(1 \pm \frac{\Delta V_0}{V_0}\right)}{(1-\varepsilon_1)} \tag{1}$$

where, A_0 is the initial cross-sectional area and ε_1 is the axial (vertical) strain in the brash ice sample. The change in circumference is later used to calculate volumetric strain as:

$$\varepsilon_V = \frac{\Delta V}{V} = \frac{V - V_0}{V_0} = \frac{r_3^2 - r_0^2}{r_0^2} \tag{2}$$

where, V and V_0 are the final and initial volumes of the brash ice sample, r_0 is the initial radius and r_3 is the equivalent radius used in volume calculation. The assumptions included in the calculation of the radius of the deformed shape of the membrane are shown in Fig. 6. The change in circumference must be measured to calculate the volumetric strain and can be measured by a string potentiometer. Spencer et al. (1991) have highlighted that the fluid flow method is more reliable than the diametral and axial strain measurement method. In the current test setup, the brash ice sample size (i.e., rubber membrane cylinder volume) is so large that the fluid flow method would be impractical. The change in circumference was instead measured with a potentiometer, i.e., wire gauge. The assumptions were made to estimate an equivalent radius of the deformed shape, as the wire gauge can only measure the change in circumference at the middle of the sample, see Fig. 6.

The equivalent radius r_3 can be calculated as follows

$$r_3 = \frac{r_1 + r_2}{2} \tag{3}$$

where,

$$r_2 = \frac{\frac{C_{tot}}{\pi} - 2t_m}{2} \text{ and } C_{tot} = (d_0 + 2t_m)\pi + \text{change in circumference} \tag{4}$$

where, C_{tot} is the total circumference, t_m is the membrane thickness = 14 mm, d_0 is the initial sample diameter and r_2 is the measured radius in the middle of the sample. The uncorrected shear stress τ_{uc} is calculated using the following equation

$$\tau_{uc} = \frac{F_H}{A} \tag{5}$$

where, F_H is the force registered by the horizontal actuator. To obtain the corrected shear stress, a rubber membrane resistance must be reduced from the uncorrected shear stress. The shear strain γ of the sample can be evaluated as follows

$$\gamma = \frac{x}{h} \tag{6}$$

where, x is the horizontal (shear) displacement and h is the height of the sample. The circumferential change in the sample was not measured during the March 2020 test campaign, so an isotropic consolidation was assumed for further calculations. The normal load causes the brash ice sample to consolidate and dimensions differ from its original dimensions as the volume of the sample changes. These dimensions can be determined approximately assuming that the sample remains cylindrical and it behaves isotropically. For isotropic consolidation, the volumetric strain (ε_V) is three times the normal strain (ε_{zz}). Then, eq. (2) can be rearranged to estimate volumetric change (ΔV) as follows

$$\Delta V = \frac{\varepsilon_{zz}}{3} V_0 \tag{7}$$

The axial strain is expressed as:

$$\varepsilon_{zz} = \frac{F_V}{E_{ice} \pi {r_1}^2} (1 - 2\nu) \tag{8}$$

where, F_V is the axial force exerted on brash ice sample, r_1 is the initial radius of the sample and E_{ice} is the elastic modulus of brash ice. The radial strain ε_{rr} is the change in the circumferential measurement of the sample, and the hoop strain $\varepsilon_{\theta\theta}$ is a change in the radius of the sample. Whereas, the axial stress σ_{zz} in the brash ice sample is given by

$$\sigma_{zz} = \frac{F_V}{\pi {r_1}^2} \tag{9}$$

The lateral constraining pressure P_b applied horizontally on the side of the sample can be calculated as

$$P_b = -\left(\frac{\frac{F_V}{\pi {r_1}^2}(1 - 2\nu) - \sigma_{zz}}{2\nu}\right) \tag{10}$$

So, the axial, radial, and hoop stresses can be calculated as follows

$$\sigma_{rr} = -P_b \quad \sigma_{\theta\theta} = -P_b \tag{11}$$

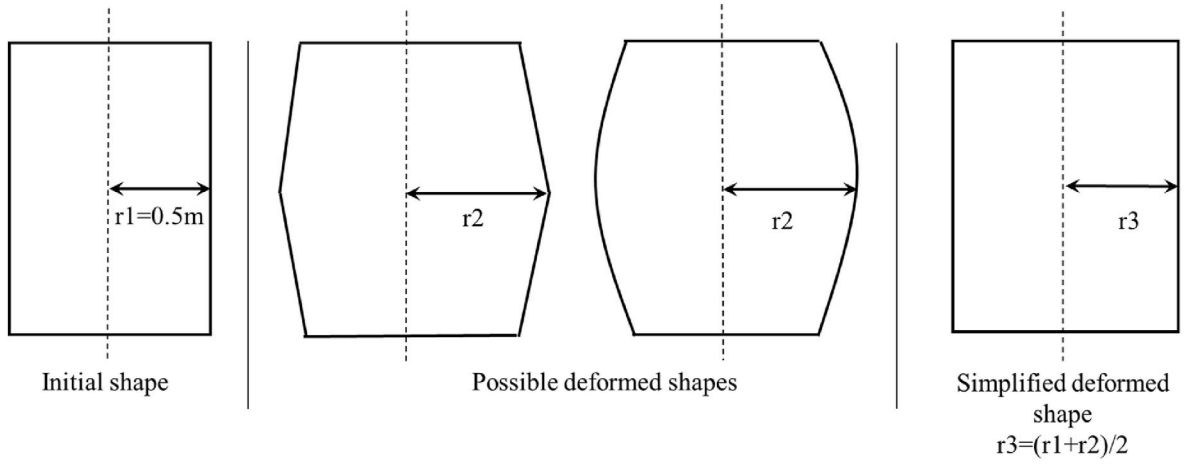

Fig. 6. The assumptions included in the calculation of the radius of the deformed shape.

Please refer to Appendix A for the derivation of the above equations. All stress and strains were calculated in cylindrical coordinates and a transformation to the cartesian coordinate system was performed. The expression used in transformation is given below:

$$\begin{bmatrix} \sigma_{xx} & \sigma_{xy} & \sigma_{xz} \\ \sigma_{yx} & \sigma_{yy} & \sigma_{yz} \\ \sigma_{zx} & \sigma_{zy} & \sigma_{zz} \end{bmatrix} = \begin{bmatrix} \cos\theta & -\sin\theta & 0 \\ \sin\theta & \cos\theta & 0 \\ 0 & 0 & 1 \end{bmatrix} \begin{bmatrix} \sigma_{rr} & 0 & \tau \\ 0 & \sigma_{\theta\theta} & 0 \\ \tau & 0 & \sigma_{zz} \end{bmatrix} \begin{bmatrix} \cos\theta & \sin\theta & 0 \\ -\sin\theta & \cos\theta & 0 \\ 0 & 0 & 1 \end{bmatrix} \tag{12}$$

3. Results and analysis

The test matrix is given in Table 1. The brash ice sample parameters are given in Table 2. Before the application of normal loading, the blocks were compressed manually to get a flat surface on the top, and then the normal load was applied to set a constant level. This ensured the proper loading of the sample. The calculated macro-porosity for sample ice collected in the year 2020 was higher than in the year 2021. In the year 2020, the brash ice was compressed further after filling the rubber membrane. This resulted in a stronger sample. As the crane was used to collect the brash ice, smaller blocks have likely to fall off. The ice block size distribution inside the rubber membrane is mostly uniform. The manual crushing of brash ice samples affected the block size distribution causing lower macro-porosity in the year 2020. The block size distribution was not measured in the year 2020. However, from the measurements of the ice blocks stored in the freezing box, the ice size before crushing was around 1 m (as limited by the crane's scoop size). After crushing, the ice block size varied between 20 and 200 mm in both years.

In the year 2021 measuring campaign, the first three cycles of horizontal stroke were registered together. The lower temperatures were observed before shearing and the higher temperatures after the cycles were completed. Fig. 7 shows the evolution of forces, actuator strokes (displacements), sample height, circumference, and stress-strain over the entire duration of cycles # 1-1, 1–2, and 1–3. The vertical force has negative values due to the downward direction of stroke. It is considered that compaction leads to denser packing, thus resulting in higher interarticular contact forces. The vertical force was changed in the third run (i.e., cycle # 1–3) from 7 kN to 3 kN. The change in sample height and circumference during test runs is shown in Fig. 7 (c) and Fig. 7 (d) respectively, where a negative value indicates a reduction and a positive value indicates a gain.

In the fourth run (i.e., cycle # 1–4) the vertical force was set to 3 kN and the sampling rate was increased to 25 Hz. But due to some technical problems, data was not registered, so it is not reported in this paper. In the fifth cycle, data for the forward stoke was registered, see Fig. 8. In this cycle, the sampling rate was lowered to 10 Hz and the horizontal actuator speed was 3.3 mm/s.

In the measuring campaign of the year 2020, two cycles were performed on the same sample of ice. In both cycles (i.e., cycle # 2-1 & 2-2), a vertical force was held constant at 15 kN during shearing, the speed of the horizontal actuator was 0.33 mm/s and the sampling rate was 1 Hz. Fig. 9, shows the evolution of forces, stroke, and change in height for cycle # 2-1. Towards the end of this cycle, the vertical force was not constant due to pressure inside the cylinder, the top plate was backing up. All runs in this cycle didn't register force plateau. So, it is safe to assume that the peak in shear force does not represent the maximum shear stress. However, if a further horizontal displacement had been applied under constant vertical force, it may have been possible to achieve a maximum shear force. Both, vertical and horizontal forces kept rising, see Fig. 9 (a). This caused a deviation from the constant vertical force and the test was stopped. The shear cylinder was moved back to its original position by applying horizontal force in opposite direction. The measured temperature of ice was −0.5°C and melting was observed.

The evolution of forces, stroke and change in height for the forward stroke of cycle # 2-2 are shown in Fig. 10. In this run, a 100 kN vertical force was applied for 200s to compress the brash ice sample. Then the vertical force was lowered to zero by creating space between the platen and the ice. Before the application of the horizontal force, the vertical force was set at a constant level of 15 kN. The test was stopped before failure could occur or reached maximum horizontal force to prevent any damage to the loading mechanism.

Table 1
Test matrix.

Year	Cycle #	Stroke Direction	Normal Force (constant level) [kN]	Sampling rate [Hz]	Speed of horizontal actuator [mm/s]
2021	1–1	Forward	7	1	0.33
		Return	7	1	0.33
	1–2	Forward	7	1	0.33
		Return	7	1	0.33
	1–3	Forward	3	1	0.33
		Return	3	1	0.33
	1–4	Forward	3	25	0.33
		Return	3	25	3.3
	1–5	Forward	3	10	3.3
2020	2–1	Forward	15	1	0.33
		Return	15	1	0.33
	2–2	Forward	15	1	0.33
		Return	15	1	0.33

Table 2
Test parameters.

year	Macro-porosity [%]	Height of sample [mm]	Air temperature [°C]	Brash ice Temp. during testing [°C]	Block sizes[a] [mm]
2021	29	815	−5	−0.3 to −1	70 to 870[1]
2020	20	936	−15	−0.5 to −2.5	50 to 1000

[a] These measurements were taken before crushing the blocks.

3.1. Stresses and strains

Further, post-processing was done to calculate shear area, shear stress, shear strain, axial strain, and volumetric strain, based on equations presented in an earlier section of this paper. The time between shearing started and until a peak in the forward stroke was selected to plot the stress-strain curve. The corrected and uncorrected shear stresses were plotted along with axial stress, see Fig. 11. The shear stress response is nonlinear to the shear strain. In Fig. 12 response of shear stress for all forward cycles is shown. In cycles # 1–3 and 1–5, the vertical force was set to 3 kN, which has been reflected in registering the lowest shear force in this test campaign. In the triaxial compression test, as stated by Singh and Jordaan (1996), the peak stress is a function of competing mechanisms related to pore collapse and brittle failure. Similarly, the shear stress in the current tests can be a function of the breaking of freeze bonds, the frictional sliding mechanism, and the crushing of ice blocks. In each testing cycle the brash ice sample went through loading and unloading phases, which caused the formation of sliding planes.

Initially, there was a decrease in the volume due to compaction at low strains, but an almost linear increase in the volume due to shearing was registered at large strains, see Fig. 13. The change in height is not equal to the change in circumference. This anisotropy is believed to be due to the method of sample preparation and the way the change in the circumference was measured. The ice sample is likely to get stronger in the vertical direction than in lateral direction due to arrangements of ice blocks.

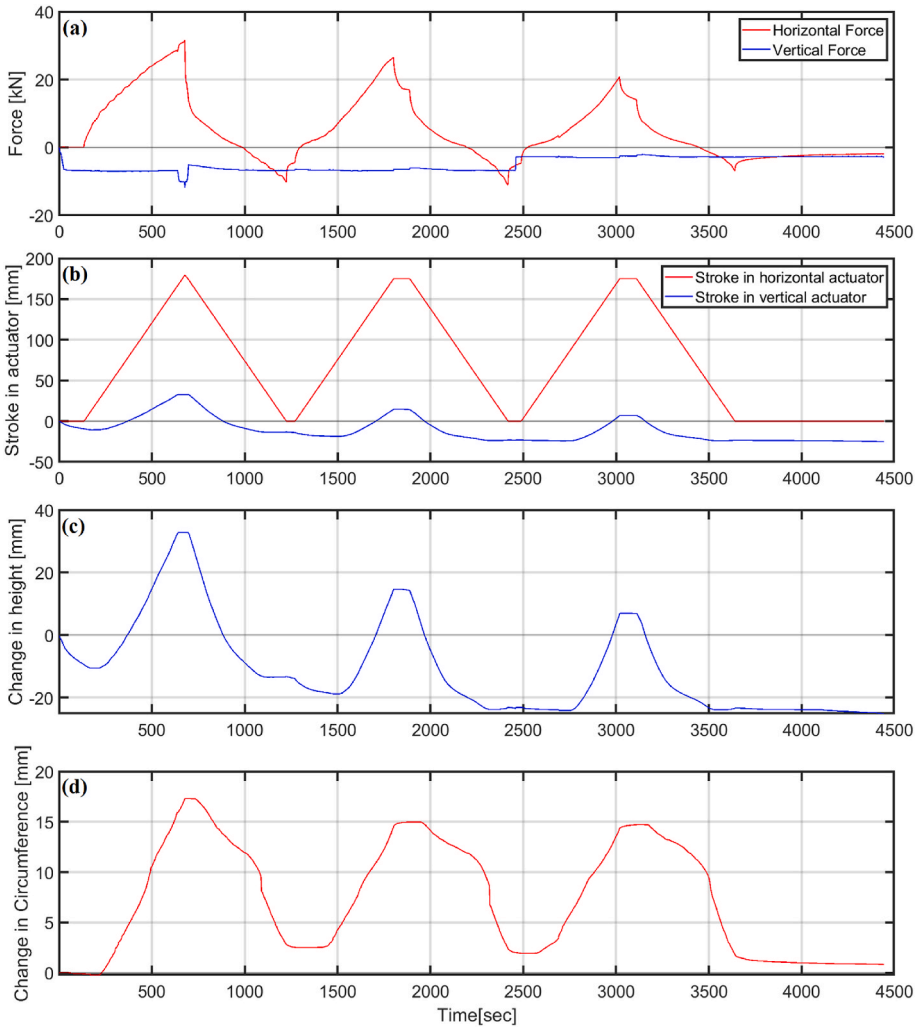

Fig. 7. Showing the evolution of (a) force, (b) actuator strokes (displacement), (c) change in height, and (d) circumference during cycles # 1-1, 1–2, and 1–3.

Similarly, the change in height versus shear strain for the forward stroke of cycle # 2-1 and 2-2 is given in Fig. 14. The effect of compaction before shearing is visible. During cycle # 2-1, the vertical force is not constant towards the end of the cycle. So that part is excluded in the performed post-processing. In cycle # 2-2, the brash ice sample was compressed for 200s with a 100 kN vertical force, so it was able to withstand higher strain in further testing.

The percentage of the volumetric strain against axial strains of forward strokes of cycle # 1-1 and # 2-1 is given in Fig. 15. The difference between volumetric strain can be associated with the difference in macro-porosity. As the brash ice sample in cycle # 2-1 was compressed before the test, resulting in the denser packing of ice blocks. Therefore, the volumetric strain in cycle # 2-1 was smaller than in cycle # 1-1 for the same axial strain.

3.2. Estimation of material model parameters

One of the goals of this experimental investigation was to calibrate a material model which represents the brash ice in the simulation of its interaction with structures. The behaviour of brash ice under load depends on both individual ice blocks and the collective/aggregate behaviour of ice blocks. The major obstacle in the development of an accurate and reliable material model of brash ice is the complexity involved in constitutive behaviour. Traditionally, the Mohr-Coulomb yield criterion and the Drucker–Prager yield criterion were the choices for the material model for ice rubble. But Kulyakhtin and Høyland (2015) have shown that the Mohr-Coulomb yield criterion cannot be used to define the shear strength of the ice rubble where high values of the angle of internal friction are involved. In addition, cohesion-less ice rubble exhibits a volumetric change behaviour which cannot be explained by the Mohr-Coulomb criterion. Wong et al. (1990) have proposed a constitutive model for broken ice based on triaxial compression test data. They have identified the need for yield surface limiting the strength along the hydrostatic axis, often termed as a Cap. They also highlighted that the initial strength of broken ice is dependent on the void ratio. Singh and Jordaan (1999) have investigated various aspects of constitutive modelling of crushed ice using triaxial compression test data. Furthermore, Heinonen (2004) have proposed a shear cap material model for the first year ridge keel and calibrated the same based on the in-situ punch through the test.

In this paper, the material model parameters of the Continuous Surface Cap Model (CSCM) are estimated based on presented large-scale shear test data. The CSCM was developed by Schwer and Murray (1994) and implemented by Schwer and Murray (2002). The CSCM was implemented to simulate the behaviour of ice rubble in the keel part of a first-year ridge in punch through test by Patil et al. (2015) and to simulate the behaviour of brash ice in pull-up test by Patil et al. (2021). A detailed theoretical description and comprehensive calibration procedure of CSCM are given elsewhere, see Murray (2007) and Jiang and Zhao (2015). The CSCM model combines the shear failure surface with isotropic cap hardening surface smoothly by using a multiplicative formulation. The general shape of the yield surface in the meridional

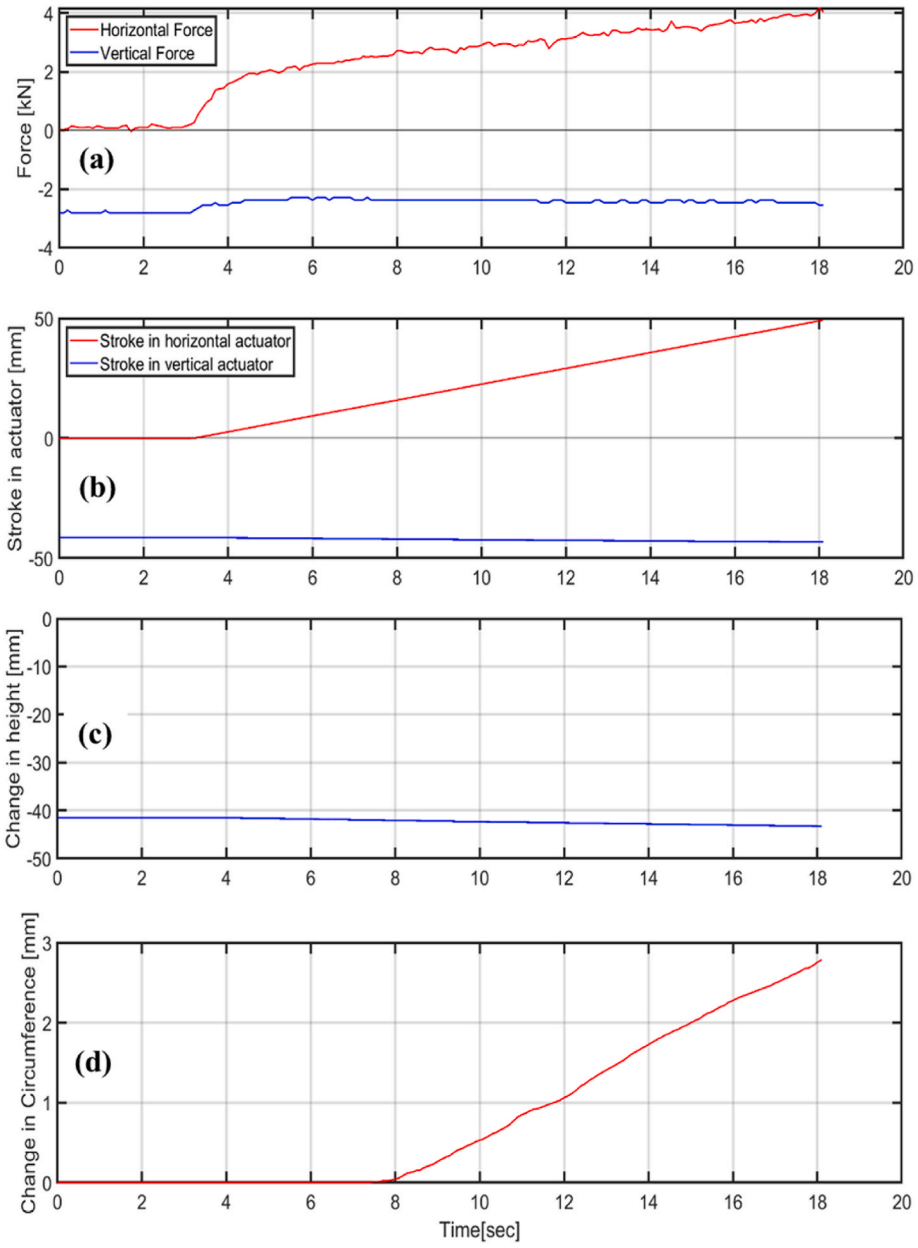

Fig. 8. Showing (a) the evolution of force, (b) actuator strokes (displacement), (c) change in height, and (d) circumference during forward stoke of cycle # 1–5.

plane is shown in Fig. 16.

This smooth cap surface provides a reduction in computational time and an advantage over numerical instability. Detailed formulation can be found in Murray (2007), so only a brief description is given here. The smooth cap model, shown in.

Fig. 16, is formed by multiplying together the failure and hardening surface functions to form a smoothly varying function given by

$$f(I_1, J_2, \kappa) = J_2 - F_f^2 . F_C \tag{13}$$

where J_2 is the second invariant of the deviatoric stress tensor. The shear failure surface (F_f) is defined as

$$F_f(I_1) = \alpha - \lambda \exp^{-\beta I_1} + \theta I_1 \tag{14}$$

where I_1 is the first invariants of the stress tensor, and α, θ, λ and β are model parameters used to match the triaxial compression. The isotropic cap hardening surface (F_c) of the model is based on a non-dimensional functional form, given below

$$F_c(I_1, \kappa) = 1 - \frac{[I_1 - L(\kappa)].[|I_1 - L(\kappa)| + I_1 - L(\kappa)]}{2[X(\kappa) - L(\kappa)]^2} \tag{15}$$

where κ is a hardening parameter that controls the motion of the cap surface and $L(\kappa)$ and $X(\kappa)$ define the geometry of the cap surface, see.

Fig. 16. Eq. (15) represents the elliptical cap that intersects the shear surface at $I_1 = L(\kappa)$. The cap expands (i.e. $X(\kappa)$ and κ increases) when plastic volume compaction occurs, and the cap shrinks (i.e. $X(\kappa)$ and κ decreases) when plastic volume dilation occurs. The evolution of the cap's motion is defined by the isotropic hardening rule, given below

$$\varepsilon_v^p = W\left(1 - e^{-D_1(X - X_0) - D_2(X - X_0)^2}\right) \tag{16}$$

where is the plastic volumetric strain, W is the maximum plastic volumetric strain, X_0 is the initial intercept of the cap surface, R is the cap aspect ratio and D_1 and D_2 are the linear and quadratic shape parameters respectively and determine the shape of the pressure volumetric strain curves. So, CSCM requires the five input parameters, i.e., X_0, W, D_1, D_2,

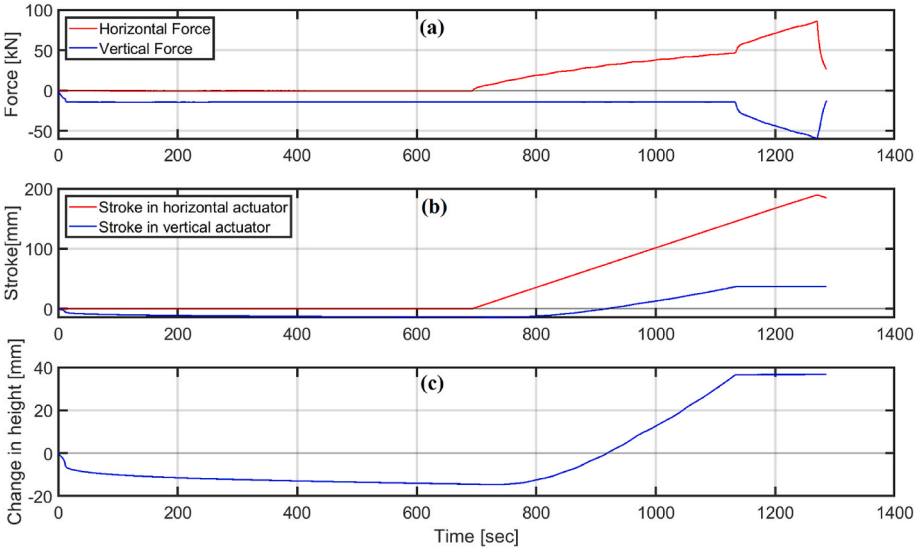

Fig. 9. Showing force vs time, actuator strokes (displacement) vs time and change in height vs. time for the forward stroke of cycle # 2-1.

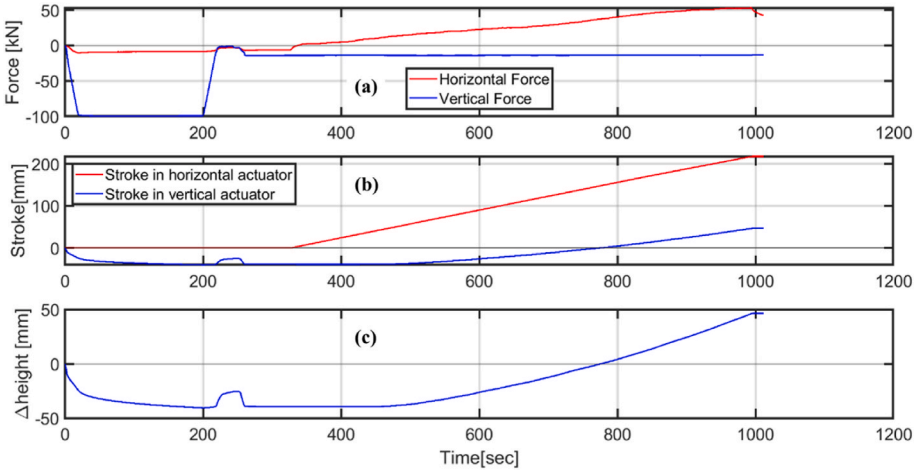

Fig. 10. Showing force vs. time, actuator strokes (displacement) vs. time, and change in height vs. time for the forward stroke of cycle # 2-2.

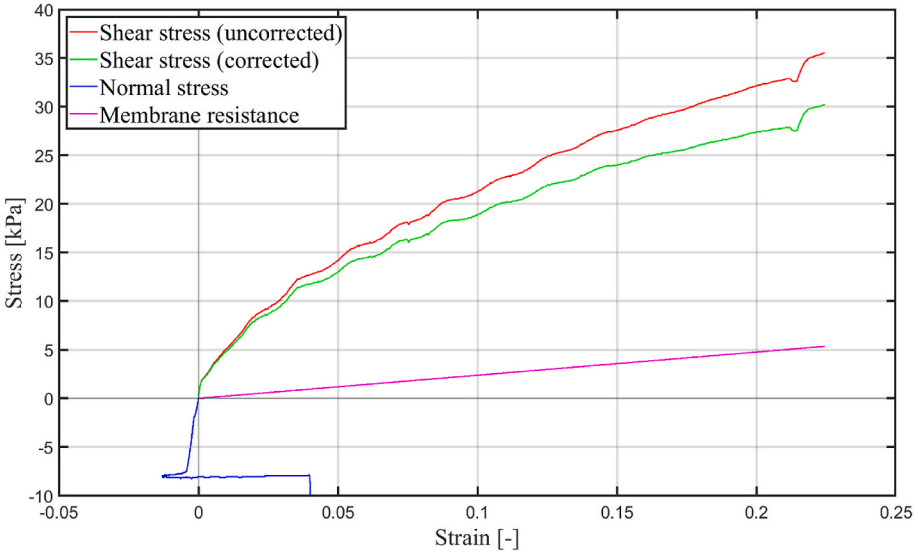

Fig. 11. Shear stress vs. shear strain curve during the forward stroke of cycle # 1-1.

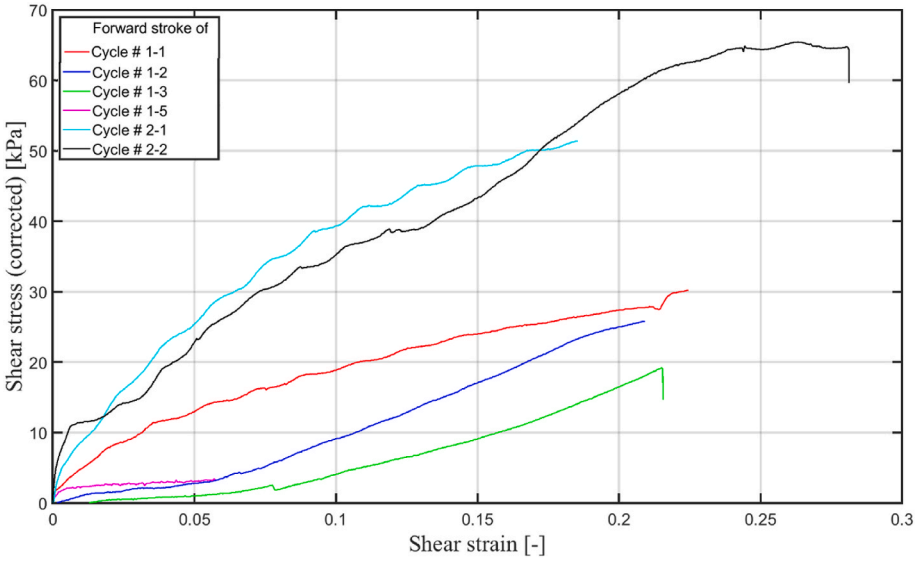

Fig. 12. The corrected shear stress-shear strain curve for forward strokes of cycle #1-1, 1–2, 1–3, 1–5, 2-1, and 2-2.

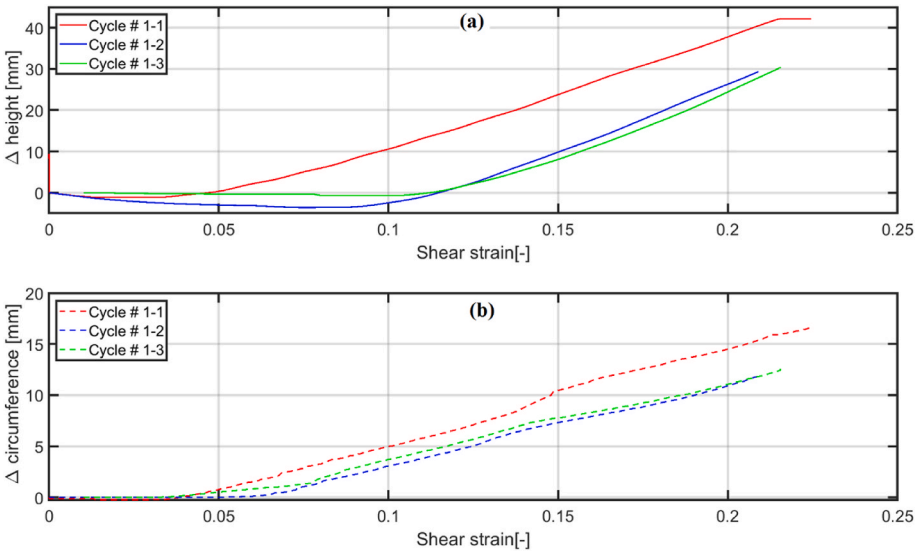

Fig. 13. (a) Change in height and (b) change in circumference vs. shear strain for forward stokes of cycle # 1-1, 1–2, and 1-3.

and *R*, to define hardening function and can be determined from hydrostatic compression and uniaxial strain tests. In addition to the inclusion of the volumetric hardening of the cap surface, the CSCM includes kinematic hardening of the shear surface. As shown by Urroz and Robert (1987), Heinonen (2004) and Serré et al. (2011), that ice rubble becomes soft during the shearing process due to dilatation. Furthermore, the hardening or softening behaviour of the material depends on the volumetric plastic strain. The hardening of the ice rubble can be observed in between first and second shear mode, see Fransson and Sandkvist (1985). The granular material such as soil exhibits nonlinearity and dilation prior to the peak under shear loading, which can be described by the kinematic hardening. The kinematic hardening is assumed to occur only in shear. Therefore, this behaviour is modelled into CSCM by introducing a multiplication factor for the shear surface. The initial shear yield surface (*Ff*) is multiplied by factor N_H, which assumes hardening of the surface until it coincides with the ultimate shear yield surface, see Fig. 17.

Fig. 17 shows the working of N_H where $\sqrt{J_{2F}}$ is the final location of the yield surface whereas $\sqrt{J_{2H}}$ is the initial location of the yield surface.

When kinematic hardening formulation is used, Eq. (14) is modified as follows:

$$F_f(J_1) = N_H\left(\alpha - \lambda \exp^{-\beta J_i} + \theta J_1\right) \tag{17}$$

The value of N_H is the distance between the failure surface and the initial yield surface along the $\sqrt{J_2}$ axis. The value of N_H can be estimated as follows

$$N_H = \sqrt{J_{2F}} - \sqrt{J_{2H}} \tag{18}$$

One additional parameter, C_H needed to be defined to include kinematic hardening in the CSCM. This parameter determines the rate of hardening and is an implicit function of the slope of the plastic shear stress-strain curve. The values of parameters (N_H and C_H) must be found by trial and error and requires a good judgment of the user to identify elastic and plastic regions of the stress-strain curve, see Isenberg et al. (1978). Further, the shear modulus (*G*) and elastic modulus (*E*) can be estimated based on the following relationship.

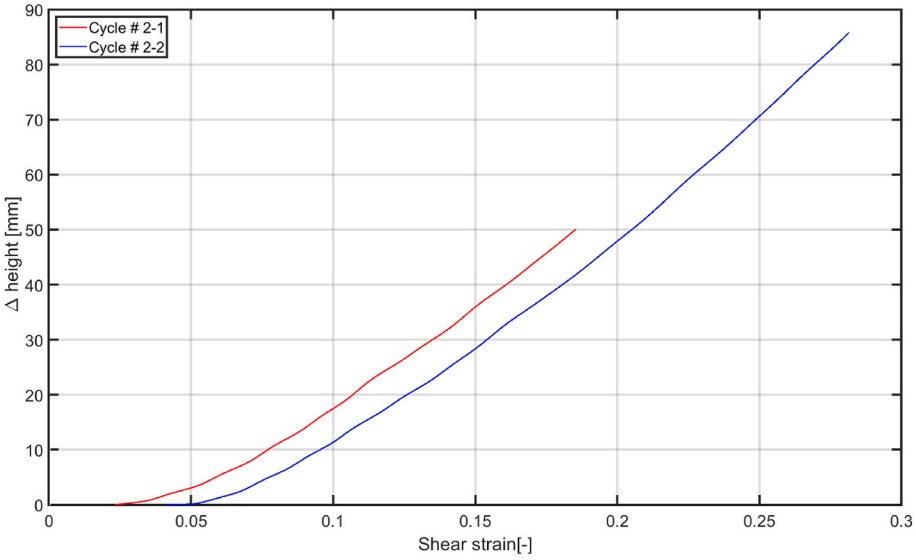

Fig. 14. Change in height vs. shear strain for forward stokes of cycle # 2-1 and 2-2.

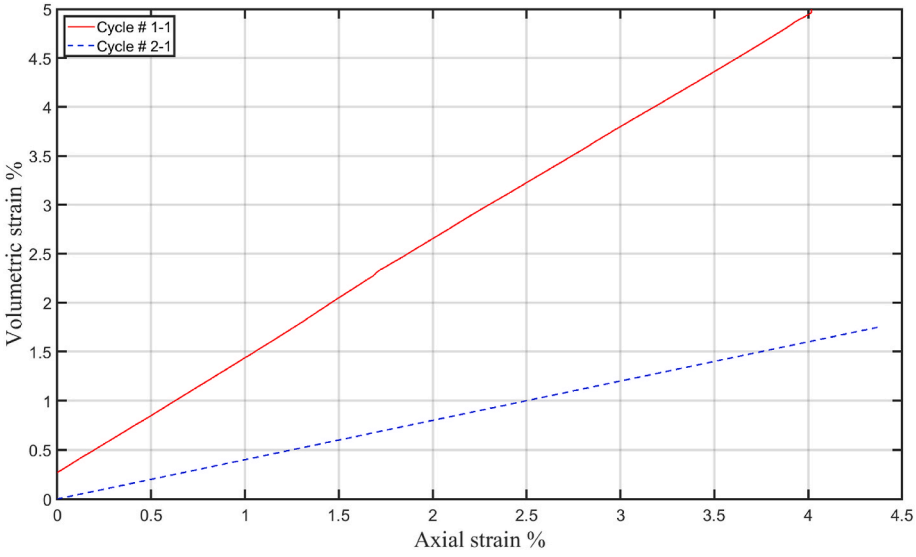

Fig. 15. Percentage volumetric strain vs. percentage axial strain of forward strokes of cycle # 1-1 and 2-1.

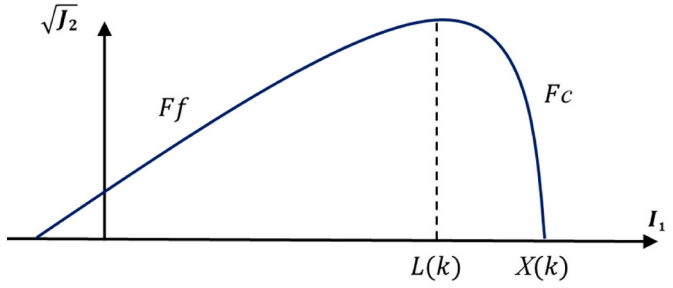

Fig. 16. General shape of the CSCM model yield surface.

$$K = \frac{E}{3(1-2\upsilon)}, G = \frac{E}{2(1+\upsilon)} \tag{19}$$

where υ is the Poisson's ratio and set equal to 0.3. During the first stage of sample preparation, the sample was compressed axially, which is similar to triaxial compression. The end of this compression was

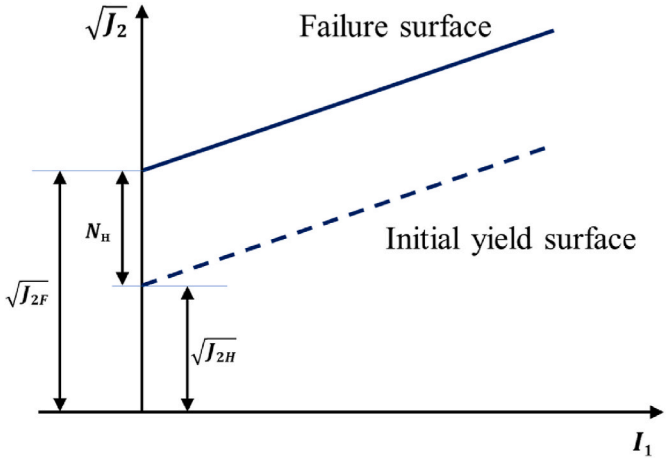

Fig. 17. Original failure surface and translating yield surface.

postulated to be the yield point of the brash ice sample, see Fig. 18. Thus, the initial rapid rise was assumed to be representative of elastic behaviour. The bulk modulus (k) was then adjusted to fit the linear elastic part of the pressure-volume curve.

The triaxial compression surface constant term (α) and linear term (θ) were estimated based on fit to the laboratory shear box tests on brash ice data presented by Fransson and Sandkvist (1985). The initial location of the cap (X_0), determines the pressure at which compaction initiates in isotropic compression. The cap aspect ratio (R), combined with the initial location of the cap (X_0), determines the pressure at which compaction initiates in uniaxial strain. So, the initial location of the cap (X_0) is the position on I_1 axis where the outer edge of the ellipse intersects. The maximum plastic volume strain (W) sets the limit strain at which all the voids will compact fully. Based on the estimation given by Wong et al. (1990) and Heinonen (2004), a value of 0.03 was selected for W. However, this estimation is highly dependent on the type of ice, loading condition and blocks shape and size distribution. Thus, numerical simulations are needed to study the effects of W. The D_1 and D_2 are material parameters determining the shape of the pressure volumetric strain curve. They were adjusted to fit the volumetric compression part of the pressure volumetric strain curve. The CSCM yield surfaces can be plotted based on the parameters estimated above. In Fig. 19, yield surfaces for two samples of cycle # 1-1 and cycle # 2-1 are shown with fitted laboratory shear box tests data, assuming that shear is the predominant failure mode.

The cyclic loading response of ice sample in 2021 test campaign under constant axial force was plotted in Fig. 19 for cycle # 1-1 and 1–2. The ice blocks inside the sample go through a shearing and crushing process during each loading-unloading cycle, eventually leading to compaction. For modelling this complex response of brash ice under cyclic loading, kinematic hardening parameters are needed. The kinematic hardening coefficient (N_H) was estimated based on the stress state at points marked in Fig. 20. In order to calculate kinematic hardening parameter (N_H), stress state at a first plateau point after the shear force was used as initial location of yield surface and stress state at the end of each forward cycle was used as the final location of yield surface, see Eq. (18). To estimate the hardening rate parameter (C_H), the slope of the shear stress versus plastic shear strain curve was used, see Fig. 11. The parameters estimated as input to the CSCM from test data are given in Table 3. The difference in the strength of the sample was reflected in estimated CSCM parameters. The test sample in cycle # 2-1 was stronger than the test sample used in cycle # 1–2 on account of lower macro-porosity.

The difference in the strength of the sample was reflected in estimated CSCM parameters. The test sample in cycle # 2-1 was stronger than the test sample used in cycle # 1–2 on account of lower macro-porosity. For a 7 kN axial loading, the secant elastic modulus was about 2 MPa and for a 15 kN axial loading, it was about 5 MPa. The reported values of elastic modulus for model ice rubble, based on the oedometer test and calculated as a function volumetric strain, were ranging from 0.7 MPa to 1.14 MPa, see Serré (2011). So, the values of the elastic modulus obtained through the current test setup are much higher and this difference in values can be attributed to the type of ice and boundary condition. Tests conducted by Serré (2011) and Matala (2021) on model ice suggest that scaling of the model ice is difficult. This discrepancy may be explained by this difficulty.

4. Discussion and conclusions

The properties of brash ice collected at Luleå harbour was analysed using a new version of the large-scale shear apparatus designed by LTU. Basic principles and design details of the test setup have been given. The results of the two measuring campaigns have been presented and analysed. Since the apparatus was designed to handle the deformation of larger blocks, it has been proven suitable for testing natural brash ice blocks in the laboratory. The calculated macro-porosity of samples tested in the year 2021 and year 2020 was 30% and 20%, respectively. In the year 2021, the sample was tested with an axial force of 7 kN and 3 kN, while the axial force in the year 2020 was 15 kN. The macro-porosity and confining axial force are the most influential factors in defining the strength and deformation of the brash ice. The compaction before shearing was believed to cause crushing of the ice blocks which lead to a denser packing of ice blocks. This process makes the sample stronger. The influence of compaction before shearing on the ice sample can be seen from cycle # 2-1 and cycle # 2-2. Also, the distribution of ice blocks inside the rubber membrane affects the macro-porosity calculation. The longer the exposure to the room temperate at the test facility and the axial force may have caused the melting on the contact surfaces and probably freeze bond to develop (i.e., sintering). Therefore, it is recommended to study the effect of compaction and the effect of macro-porosity, in future studies. Shear tests were conducted under drained conditions, and the shearing speed was slow enough to disperse any pore pressures that accumulated during the shearing process. Therefore, the shear strength of the sample is unaffected by pore pressure. In reality, the shear strength of brash ice may be dominated by pore water pressure. The water pore pressure effect can be studied with the same

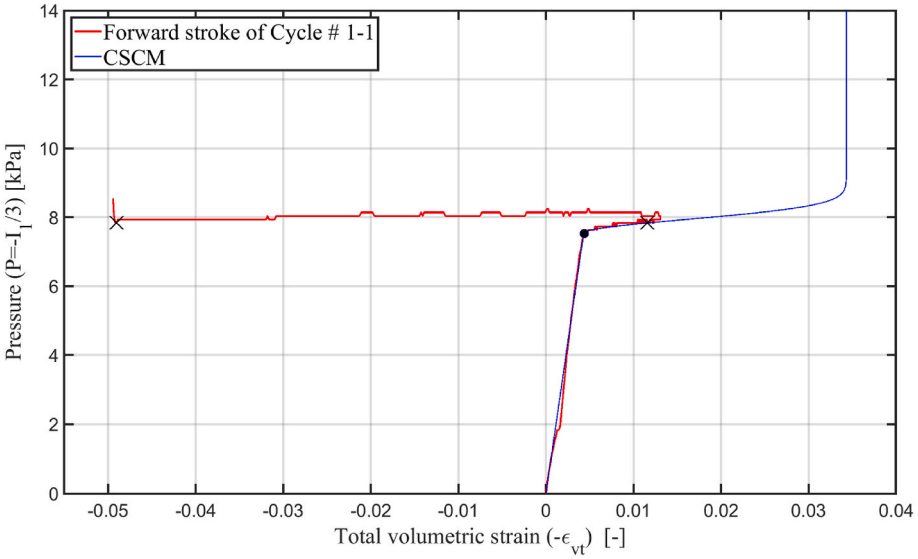

Fig. 18. The volumetric hardening function of CSCM is fitted to forward stroke of cycle # 1-1.

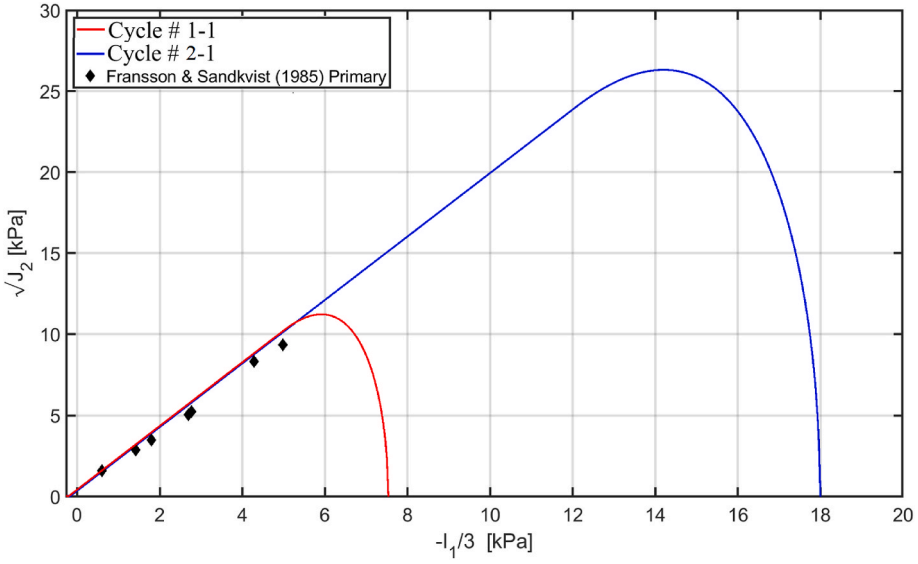

Fig. 19. The CSCM yield surface in shear meridian based on cycle # 1-1 and cycle # 2-1.

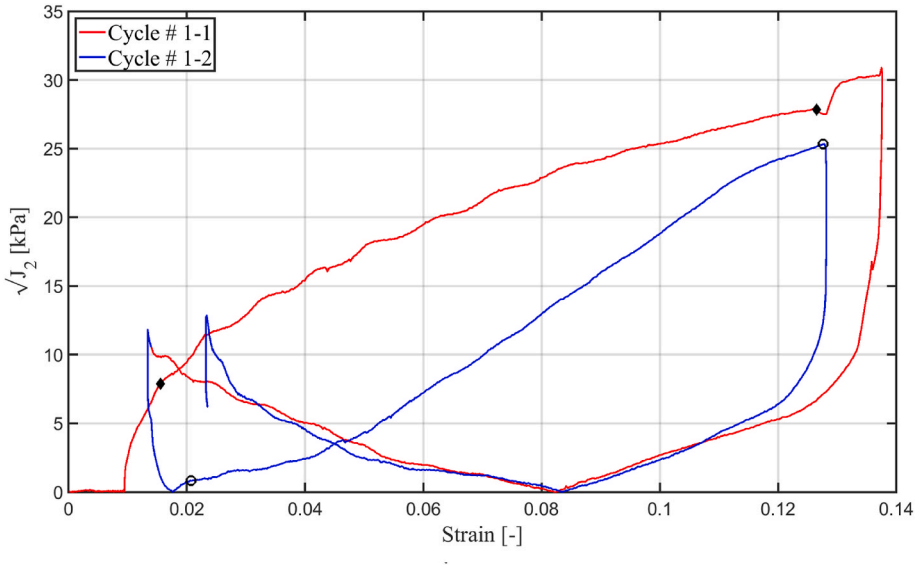

Fig. 20. Showing the 1st and 2nd cycles of the year 2021 test campaign.

Table 3
CSCM parameters.

Name of parameter	Symbol [unit*]	Cycle #1	Cycle # 6
Bulk modulus	K [MPa]	1.8	5.5
Shear modulus	G [MPa]	0.8	2.5
Shear surface Constant term	α [MPa]	6.4E-04	5.3E-04
Shear surface linear term	θ [rad]	0.96	0.96
Kinematic hardening parameter	N_H [-]	0.02	0.04
Rate of hardening	C_H [-]	0.14	0.33
Cap aspect ratio	R [-]	0.5	0.5
Cap initial location	X_o [MPa]	0.023	0.054
Maximum plastic volume compaction	W [-]	0.03	0.03
Linear shape parameter	D_1 [MPa]	0.4	0.4
Quadratic shape parameter	D_2 [MPa^2]	3E6	3E6

apparatus by using a controlled water system with a pressure device and flowmeter. Furthermore, the real brash ice channel can have different boundary conditions at the top and bottom due to repeated breaking, resulting in variable confinement. Thus, the strength of brash ice varies with depth. In addition, a different frequency of ice breaking (2020 vs 2021) causes different brash ice block sizes, shapes and microstructures, which may subsequently give different shear strength. More research is needed to support this correlation.

The use of the test data should be with care, as there might be differences between the real brash ice in the field and those used in the laboratory testing. The variation in brash ice block sizes can be notable in the field. Additionally, the inclusion of only big blocks due to the scooping size of the crane and crushing before the shearing, likely have caused some deviation from natural brash ice block sizes. Several more tests are needed to capture the spatial variation of brash ice samples. The crushing of the brash ice blocks was also likely occurring during shearing under higher stresses. Thus, it is difficult to distinguish if the compaction or the shearing caused most of the crushing. The inclusion of circumferential measurements in the measuring campaign of the year

2021 allowed to measure the volumetric strain more accurately. Even though information of circumferential changes in the middle of the sample was known, the potential error in measuring volume may be reduced by using more wire gauges.

The test data was used to estimate the yield strength, bulk and shear modulus, volumetric hardening (i.e. cap) and kinematic hardening parameters of the CSCM, see Table 3. The shear surface of CSCM was fitted based on laboratory shear box tests by Fransson and Sandkvist (1985). The estimated values of parameters have been used to visualize the CSCM yield surface in the shear meridian, see Fig. 19. The plotting of the CSCM surface confirms the difference in strength between the two samples. As shown by Wong et al. (1990), in the loose brash ice mass frictional behaviour predominates whereas in dense brash ice mass cohesion between ice blocks become more significant. The CSCM can simulate the shear and compaction behaviour of a brash ice mass. In addition, kinematic hardening parameters can be used to simulate the effect of cyclic loading. Although, more extensive test data is needed to calibrate the various additional parameters.

The presented results are significant in at least two major respects. First, this study has identified the significance of macro-porosity and axial load in this test setup. Second, this study has identified areas of improvement in test setup highlighting the need for standardization of tests involving brash ice. There are three areas of improvements suggested: sufficient no. of tests, method of sample preparation, and instrumentations.

CRediT authorship contribution statement

Aniket Patil: Writing – original draft, Conceptualization, Data curation, Investigation, Formal analysis, Validation, Visualization. **Vasiola Zhaka:** Experimentation, Data curation, Writing – review & editing. **Bjørnar Sand:** Software, Funding acquisition, Project administration, Resources, Supervision, Writing – review & editing. **Jan Laue:** Supervision, Writing – review & editing. **Andrzej Cwirzen:** Supervision, Funding acquisition, Project administration, Writing – review & editing.

Declaration of competing interest

The authors declare that they have no known competing financial interests or personal relationships that could have appeared to influence the work reported in this paper.

Acknowledgements

The authors gratefully acknowledge the financial and technical support KOLARCTIC (Project # 1867.50, KO2100 ICEOP), Nordland county, Luleå University of Technology, SINTEF, the Research Council of Norway, (project # 195153, COLDTECH), and industry partners. The staff of the Port of Luleå is thanked for their support. Special thanks to Mr. Thomas Forsberg, Research Engineer at LTU laboratories, who helped to plan and perform the tests.

Appendix A. Supplementary data

Supplementary data to this article can be found online at https://doi.org/10.1016/j.oceaneng.2022.110935.

References

Bonath, V., Zhaka, V., Sand, B., 2019. Field Measurements on the Behavior of Brash Ice.
Boroojerdi, M.T., Bailey, E., Taylor, R., 2020. Experimental investigation of rate dependency of freeze bond strength. Cold Reg. Sci. Technol. 178, 103120.
Dempsey, J.P., Palmer, A., Sodhi, D., 2001. High pressure zone formation during compressive ice failure. Eng. Fract. Mech. 68 (17–18), 1961–1974.
Ettema, R., Matsuishi, M., Kitazawa, T., 1985. Influence of ice-rubble size on resistance to ship-hull motion through a thick layer of ice rubble. In: POAC'85, 8th International Conference on Port and Ocean Engineering under Arctic Conditions.
Ettema, R., Matsuishi, M., Kitazawa, T., 1986. Model tests on ice-rubble size and ship resistance in ice rubble. Cold Reg. Sci. Technol. 12 (3), 229–243.
Ettema, R., Schaefer, J., Huang, H., 1998. Ice-tank data on brash-ice loads against barges. J. Cold Reg. Eng. 12 (3), 153–161.
Fransson, L., Sandkvist, J., 1985. Brash ice shear properties : laboratory tests. In: The 8th International Conference on Port and Ocean Engineering under Arctic Conditions : Proceedings Dansk Hydraulisk Institut, pp. 75–87. Narssarssuaq, Greenland.
Gale, A., Wong, T., Sego, D., Morgenstern, N., 1987. Stress-strain behaviour of cohesionless broken ice. In: Proceedings of the 9th International Conference on Port and Ocean Engineering under Arctic Conditions, pp. 109–119.
Greisman, P., 1981. Brash Ice Behavior. Coast guard research and development center groton ct.
Heinonen, J., 2004. Constitutive Modeling of Ice Rubble in First-Year Ridge Keel. Department of Mechanical Engineering. Helsinki University of Technology Espoo, Finland, pp. 3–142.
Heinonen, J., Määttänen, M., 2001. Full-scale testing of ridge keel mechanical properties in Loleif-project. In: Proceedings of the International Conference on Port and Ocean Engineering under Arctic Conditions.
Hu, J., Zhou, L., 2015. Experimental and numerical study on ice resistance for icebreaking vessels. International Journal of Naval Architecture and Ocean Engineering 7 (3), 626–639.
Isenberg, J., Vaughan, D., Sandler, I., 1978. Nonlinear Soil-Structure Interaction. Final Report Weidlinger Associates.
Jiang, H., Zhao, J., 2015. Calibration of the continuous surface cap model for concrete. Finite Elem. Anal. Des. 97, 1–19.
Jordaan, I.J., 2001. Mechanics of ice–structure interaction. Eng. Fract. Mech. 68 (17–18), 1923–1960.
Jordaan, I.J., Singh, S., 1994. Compressive ice failure: critical zones of high pressure. In: Proceedings, 12th International IAHR Symposium on Ice, pp. 505–514.
Jordaan, I.J., Timco, G.W., 1988. Dynamics of the ice-crushing process. J. Glaciol. 34 (118), 318–326.
Kitazawa, T., Ettema, R., 1985. Resistance to ship-hull motion through brash ice. Cold Reg. Sci. Technol. 10 (3), 219–234.
Kulyakhtin, S., Høyland, K.V., 2015. Ice rubble frictional resistance by critical state theories. Cold Reg. Sci. Technol. 119, 145–150.
Li, F., Goerlandt, F., Kujala, P., Lehtiranta, J., Lensu, M., 2018. Evaluation of selected state-of-the-art methods for ship transit simulation in various ice conditions based on full-scale measurement. Cold Reg. Sci. Technol. 151, 94–108.
Liferov, P., Bonnemaire, B., 2005. Ice rubble behaviour and strength: Part I. Review of testing and interpretation of results. Cold Reg. Sci. Technol. 41 (2), 135–151.
Matala, R., 2021. Investigation of model-scale brash ice properties. Ocean Eng. 225, 108539.
Matala, R., Skogström, T., 2017. Brash Ice Channel Research. Winter Navigation Research Board.
Mellor, M., 1980. Ship resistance in thick brash ice. Cold Reg. Sci. Technol. 3 (4), 305–321.
Murray, Y.D., 2007 May. Users manual for LS-DYNA concrete material model 159. United States. Federal Highway Administration. Office of Research, FHWA-HRT-05-062.
Patil, A., Sand, B., Fransson, L., 2015. Finite element simulation of punch through test using a continuous surface cap model. In: Proceedings of the 23nd International Conference on Port and Ocean Engineering under Arctic Conditions (Trondheim, Norway).
Patil, A., Sand, B., Fransson, L., Bonath, V., Cwirzen, A., 2021. Simulation of brash ice behavior in the Gulf of Bothnia using smoothed particle hydrodynamics formulation. J. Cold Reg. Eng. 35 (2).
Polojärvi, A., Tuhkuri, J., Pustogvar, A., 2015. DEM simulations of direct shear box experiments of ice rubble: force chains and peak loads. Cold Reg. Sci. Technol. 116, 12–23.
Pustogvar, A., Høyland, K.V., Polojärvi, A., Bueide, I.M., 2014. Laboratory scale direct shear box experiments on ice rubble: the effect of block to box size ratio. In: ASME 2014 33rd International Conference on Ocean, Offshore and Arctic Engineering. American Society of Mechanical Engineers Digital Collection.
Riska, K., Bridges, R., Shumovskiy, S., Thomas, C., Coche, E., Bonath, V., Tobie, A., Chomatas, K., de Oliveira, R.C.D., 2019. Brash ice growth model–development and validation. Cold Reg. Sci. Technol. 157, 30–41.
Sandkvist, J., 1981. Conditions in brash ice covered channels with repeated passages. In: International Conference on Port and Ocean Engineering under Arctic Conditions: 27/07/1981-31/07/1981. Universite Laval, pp. 244–252.
Schwer, L.E., Murray, Y.D., 1994. A three-invariant smooth cap model with mixed hardening. Int. J. Numer. Anal. Methods GeoMech. 18 (10), 657–688.
Schwer, L.E., Murray, Y.D., 2002. Continuous surface cap model for geomaterial modeling: a new LS-DYNA material type. In: Seventh International LSDYNA Users Conference. LSTC& ETA, Dearborn. Michigan, pp. 16–35.
Serré, N., 2011. Mechanical properties of model ice ridge keels. Cold Reg. Sci. Technol. 67 (3), 89–106.
Serré, N., Repetto-Llamazares, A.H.V., Høyland, K.V., 2011. Experiments on the Relation between Freeze Bond and Ice Rubble Strength Part1 Shear Box Experiments Proceedings of the 22nd International Conference on Port and Ocean Engineering under Arctic Conditions (Espoo, Finland).
Singh, S., Jordaan, I., 1996. Triaxial tests on crushed ice. Cold Reg. Sci. Technol. 24 (2), 153–165.
Singh, S., Jordaan, I., 1999. Constitutive behaviour of crushed ice. Int. J. Fract. 97 (1), 171–187.
Sorsimo, A., Nyman, T., Heinonen, J., Transport, F., 2014. Ship-Ice Interaction in a Channel. Winter Navigation Research Board, Helsinki. Report 93.

Spencer, P., Masterson, D., Dorris, J., 1991. The measurement of volumetric strain in triaxial testing of ice samples. In: Proceedings, 1991 Offshore Mechanics and Arctic Engineering Conference, pp. 237–244. Stavanger, Norway.
Timco, G., Funke, E., Sayed, M., Laurich, P., 1992. A laboratory apparatus to measure the behavior of ice rubble. In: Proceedings of the International Conference on Offshore Mechanics and Arctic Engineering. American Society of Mechanical Engineers, 369-369.
Tuovinen, P., 1979. The Size Distribution of Ice Blocks in a Broken Channel. Teknillinen korkeakoulu.
Urroz, G.E., Robert, E., 1987. Simple-shear box experiments with floating ice rubble. Cold Reg. Sci. Technol. 14 (2), 185–199.
Wong, T., Morgenstern, N., Sego, D., 1990. A constitutive model for broken ice. Cold Reg. Sci. Technol. 17 (3), 241–252.
Zhaka, V., Bonath, V., Sand, B., Cwirzen, A., 2020. Physical and mechanical properties of ice from a refrozen ship channel ice in Bay of Bothnia. In: Proceedings of the 25th International Symposium on Ice.